metals

MDPI

Article

Removal of Low-Content Impurities from Pure Al by Supergravity Combined with Semi-Solid Method

Lu Wang, Xi Lan, Zhe Wang and Zhancheng Guo *

State Key Laboratory of Advanced Metallurgy, University of Science and Technology Beijing, Beijing 100083, China; b20180540@xs.ustb.edu.cn (L.W.); b2211442@ustb.edu.cn (X.L.); zhewang@ustb.edu.cn (Z.W.)
* Correspondence: zcguo@ustb.edu.cn

Abstract: Recently, the purification technology for high-purity aluminum (Al) has become the focus and difficulty of the majority of researchers. In this study, a novel approach for removing iron (Fe) impurities from pure Al via combining the supergravity field and semi-solid refining was proposed. Various separation temperatures (T), holding times (t_h), and separation times (t_s) were applied within a gravitational field to explore their impact on the purification process and its underlying mechanisms. The optimal conditions were achieved at T = 653 °C, t_h = 40 min, t_s = 3 min, and a gravity coefficient G = 1000, with the loss rate of purified Al reaching up to 4.1% and the removal rate of Fe reaching 81.9%. The Fe content in pure Al was reduced from 0.32 wt.% to 0.06 wt.%. Moreover, the purified mechanism of supergravity in a semi-solid method was reported for the first time. It was concluded that supergravity could decrease the value of the effective distribution coefficient (k_e), thereby promoting the continuous migration of Fe impurities at the solidification interface into the liquid phase. The Fe-rich phase in the Al melt was completely filtered to the lower part of the crucible in the supergravity field, completing the further purification of the pure Al.

Keywords: industrial pure Al; Fe removal; supergravity; semi-solid; effective distribution coefficient (k_e)

check for updates

Citation: Wang, L.; Lan, X.; Wang, Z.; Guo, Z. Removal of Low-Content Impurities from Pure Al by Supergravity Combined with Semi-Solid Method. *Metals* **2023**, *13*, 1945. https://doi.org/10.3390/met13121945

Academic Editors: Frank Czerwinski and Antoni Roca

Received: 19 October 2023
Revised: 25 November 2023
Accepted: 26 November 2023
Published: 27 November 2023

Copyright: © 2023 by the authors. Licensee MDPI, Basel, Switzerland. This article is an open access article distributed under the terms and conditions of the Creative Commons Attribution (CC BY) license (https://creativecommons.org/licenses/by/4.0/).

1. Introduction

In nature, the conductivity of metals from high to low is silver (Ag), copper (Cu), gold (Au), and aluminum (Al). However, Ag and Au, being precious metals, have higher prices, making them less suitable for wiring. Although the conductivity of Al is only 2/3 of Cu, its density is only 1/3 of Cu. Therefore, the weight of Al wire is only half that of Cu wire for the same amount of electricity. It has gradually become an inexpensive alternative material to replace Cu cables and is widely used to make wires, cables, and conductive components in the electrical industry [1–5]. The electrical conductivity of Al is easily worsened by impurities in the matrix. In recent years, numerous researchers have dedicated substantial efforts to the research and development of the purification process for high-purity Al. Nevertheless, the capability to produce high-purity Al is currently limited to developed countries like the United States, Germany, and Japan. In China, only a handful of manufacturers possess the capacity to produce high-purity Al [6–8]. Therefore, there is an urgent imperative to intensify research and development endeavors aimed at advancing production technologies for high-purity Al within China.

At present, the methods used to purify Al with low-content impurities mainly consist of chemical methods, such as electrolysis, and physical segregation purification methods [6,9,10]. The electrolysis method primarily involves three-layer liquid electrolytic refining, while the segregation method includes vacuum evaporation, fractional crystallization, directional solidification, and zone melting methods [11]. Although three-layer liquid electrolysis is effective for large-scale purification, it is expensive and harmful to the environment due to the use of fluoride electrolytes. Therefore, this study focuses on the segregation method, also

known as the solidification purification method, which purifies Al based on the solubility of each impurity element in the liquid phase and the solid phase. Currently, directional solidification and zone smelting methods are most commonly studied [9], but they have significant drawbacks, such as high cost and a long production cycle. Duan [10] et al. used zone melting purification for high-purity Al. This indicates that the sample needs 15 times zone melting with the travel speed of the molten area at 1.0 mm/min. The obtained contents of the impurities Cu, Si, Fe, and Ti in the middle of the sample (i.e., 140 mm from the head end) were 0.9057, 0.8116, 0.1202, and 0.4237 ppm, respectively.

Fe is the most pervasive impurity element in Al alloys and is capable of forming Fe-rich phases with other elements, leading to detrimental conductivity and mechanical properties of the Al alloys [6,12]. Trace amounts of Fe impurity elements in pure Al typically form low-melting-point eutectic compounds with the matrix, making them difficult to remove. At higher purification temperatures, trace Fe impurities are thoroughly dissolved in the matrix. At lower temperatures, solid–liquid separation is theoretically possible. However, due to the increase in the matrix Al solid phase fraction in pure Al, separating the low-melting-point eutectic Fe-rich phase from the matrix through conventional means becomes difficult. Therefore, it is particularly important to address how to remove the low-melting-point Fe-rich phases from pure Al samples at lower temperatures [13,14]. Semi-solid processing for refining metal alloys was first introduced by Mehrabian [15] et al. This method involves heating the metal to the temperature range of the solid/liquid coexistence and separating the solid and liquid phases through filtration treatment [16,17], electromagnetic force [10,18–21], or gravitational sedimentation. Cho [16] et al. investigated the industrial-scale purification of A7075 wrought Al alloy under semi-solid conditions using a servo press. It was confirmed that the purity of Al reached up to 95% at the semi-solid temperature of 620 °C, with an extrusion ratio of 3 and an extrusion speed parameter of 25 mm/s. Additionally, supergravity can effectively enrich and segregate alloys with high levels of solid phase impurities at elevated temperatures due to its strong physical force, such as Al [22–24]. Sun [22] et al. investigated the separation behavior of Al_2O_3 particles and the prematurely precipitated Fe-rich phase around the Al_2O_3 particles in the purification of primary Al liquid using supergravity technology. Although, Zhao [23] et al. used the supergravity field to enrich the low-content impurities from pure Al and efficiently sediment the Fe and Si impurities. However, it is noteworthy that the impurities were merely concentrated at the bottom of the samples and not separated from the Al matrix, which means the treated sample needed further treatment to separate these impurities using mechanical or chemical methods.

Herein, we investigated a novel method that combines the supergravity field with the semi-solid state to purify Al, reducing low-content impurities. This method enables the one-step removal of inclusions. Specifically, pure Al is heated to a semi-solid state, inducing the matrix Al to solidify, while the Fe-rich impurities exist in a liquid phase. Under the influence of a supergravity field, these impurities are expelled from the matrix, thereby accomplishing the purification of pure Al. The results show that under the conditions of G = 1000, T = 653 °C, t_h = 40 min, and t_s = 3 min, the Fe content decreased from 0.32 wt.% to 0.06 wt.%, with the removal rate of Fe reaching 81.9%.

2. Materials and Methods

In this study, 1060 industrial pure Al was selected as the research subject. It contains a small amount of Fe (0.32 wt.%) element, which is a typical conductive material. The composition of the raw material was determined by ICP-OES analysis, and the results are listed in Table 1. The supergravity field generated by a centrifugal apparatus is illustrated in Figure 1, along with the schematic of the experimental apparatus. This supergravity metallurgical experimental setup was adapted from the DL-8M model of a medical centrifuge manufactured by Shanghai Luxiangyi Centrifuge Instrument Co., Ltd. (Shanghai, China), comprising a heating furnace and a counterweight furnace. Both furnaces were fixed into the centrifugal rotor. A composite graphite crucible containing a porous support plate was

applied to accomplish the separation process. The graphite felt, with a thickness of 5 mm, a diameter of 20 mm, and a volume density of 0.12–0.14, was employed as the filter.

Table 1. Chemical composition of 1060 industrial pure Al.

Element	Fe	Si	Cu	Al
Content/wt %	0.32	0.02	<0.05	Bal.

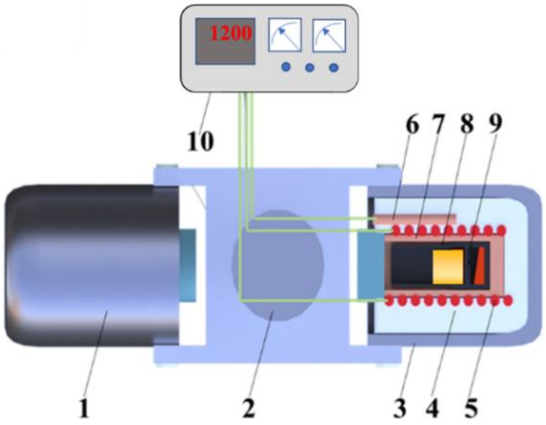


Figure 1. Schematic of the centrifugal apparatus: (1) Counterweight, (2) Centrifugal axis, (3) Heating furnace, (4) Refractory materials, (5) Resistance coil, (6) Thermocouple, (7) Furnace chamber, (8) Graphite crucible, (9) filter, and (10) temperature controller.

The gravity coefficient (G) was calculated as the ratio of the centrifugal acceleration to the normal gravity acceleration (as shown in Equation (1)).

$$G = \frac{\sqrt{g^2 + (\omega^2 r)^2}}{g} = \frac{\sqrt{g^2 + (\frac{N^2 \pi^2 r}{900})^2}}{g} \quad (1)$$

where w is the angular velocity (in rad·s^{-1}), N is the rotating speed of the centrifuge (in r·min^{-1}), r is the distance from the axis to the center of the sample (r = 0.25 m), and g is the normal gravity constant.

The experimental procedure is as follows. Blocks of 1060 industrial pure Al with a diameter of less than 20 mm and a height of 30 mm were selected. The blocks were heated at 648 °C, 653 °C, or 658 °C for a duration of 20–60 min. Following the heat preservation, the supergravity apparatus was turned on and operated at an angular velocity equal to 1892 rpm (G = 1000). After the supergravity apparatus was shut off, prompt water quenching was employed to maintain its as-cast structure. Reference samples were obtained using the same method but under normal gravity conditions (acceleration 1 g). The morphology of the samples was investigated through scanning electron microscopy coupled with an energy-dispersive spectroscope (SEM-EDS, MLA 250, New York, NY, USA). The chemical composition of the inclusions was characterized by inductively coupled plasma-optical emission spectroscopy (ICP-OES, Optima 7000DV, New York, NY, USA). The solidification path of 1060 industrial pure Al was simulated by the Scheil solidification model in Thermo-Calc software (USTB MatCom of Beijing Advanced Innovation Center for Materials Genome Engineerin).

3. Results and Discussion

3.1. Separation of Fe Impurity from Pure Al

Figure 2 presents the SEM images of the original material with marked analyzed phases, and their corresponding elemental compositions are listed in Table 2. It can be seen that the gray phase represents the Al matrix, while the gray and white spherical eutectic

particles correspond to the Fe-rich phase. At the grain boundary, the white particles were the $Al_{13}Fe_4$ phase, composed of 76.80 at.% Al and 23.20 at.% Fe. Additionally, the black areas denote the presence of shrinkage holes in the raw material.

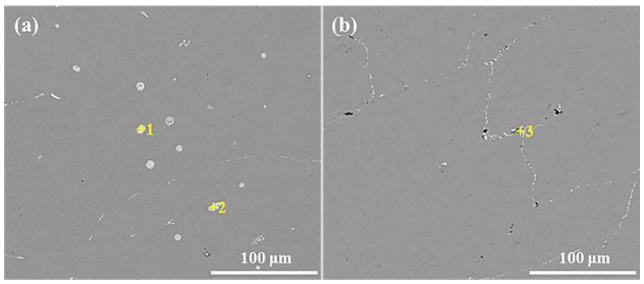


Figure 2. SEM images of the original material of pure Al at different positions (**a**) and (**b**).

Table 2. EDS analysis of components marked with numerical symbols in Figure 1.

No.	Al (at.%)	Fe (at.%)	Phase
Pt. 1	85.75	14.93	Fe-rich
Pt. 2	88.61	11.39	Fe-rich
Pt. 3	76.80	23.20	$Al_{13}Fe_4$

The Scheil solidification model in Thermo-Calc was employed to obtain the solidification path of 1060 industrial pure Al in this study, as shown in Figure 3. The results indicate that the α-Al phase started to solidify at 658 °C, followed by the $Al_{13}Fe_4$ phase at 648 °C. Subsequently, the Al_8Fe_2Si phase precipitated at 646 °C, and the temperature decreased to 629 °C, at which point the industrial pure Al was completely solidified. Therefore, traditional supergravity separation techniques (utilizing density differences between different phases in a high-temperature molten state for impurity removal) have limited efficacy and cannot accomplish one-step separation. To achieve the solid–liquid separation of the sample and, thereby, purify the industrial pure Al, the subsequent experimental temperatures were set between 648 °C and 658 °C. Specifically, the Al matrix serves as the solid phase, while the Fe-rich impurities act as the liquid phase. However, as observed in Figure 3, within this temperature range, the solid phase in the sample is relatively high and the natural settling time is long. Previous studies [15] have revealed that during the solidification of the sample when the solid phase fraction reaches 0.2, dendritic networks begin to form (interpreted as a continuous solid skeleton). The permeability and fluidity of the mushy zone decrease. When the solid phase fraction exceeds 0.2, it results in the hard separation of the liquid phase at the grain boundaries from the matrix under normal gravity. Techniques such as squeezing or other methods are necessary to allow the interdendritic liquid to flow out from the dendritic network. Therefore, this section proposes a semi-solid supergravity method for purifying industrial pure Al, that is, the liquid Fe-rich impurity phase is separated from the Al sample under the supergravity field.

To evaluate the effects of these conditions on the experimental efficiency, several parameters, including the experimental liquid fraction that can be separated (F_L), the loss rate of the purified Al (R_{Al}), and the removal rate of Fe (η_{Fe}) were defined (as shown in Equations (2)–(4)).

$$F_L = \frac{m_f}{m_r + m_f} \times 100\% \tag{2}$$

$$R_{Al} = \frac{m_f - \left(m_f \times \omega_{Fe}\right)}{m_r + m_f} \times 100\% \tag{3}$$

$$\eta_{\mathrm{Fe}} = \frac{m_f \times \omega_{Fe_f}}{m_r \times \omega_{Fe_r} + m_f \times \omega_{Fe_f}} \times 100\% \tag{4}$$

where m_r is the mass of the remaining Al left in the upper crucible, m_f is the mass of the filtered Al collected in the lower crucible, and ω_{Fe_r} and ω_{Fe_f} are the Fe content (wt.%) in the remaining and the filtered Al, respectively.

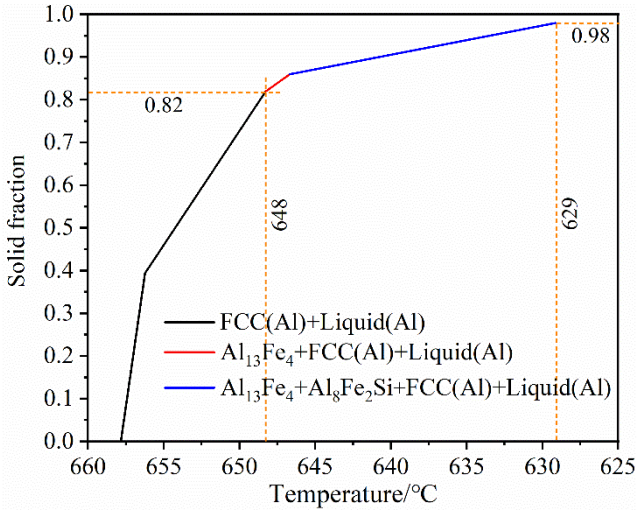


Figure 3. Solid fraction vs. temperature for pure Al, calculated using the Thermo-Calc Scheil solidification module.

The 1060 industrial pure Al was purified under conditions including the holding time (t_h), separation temperature (T), and separation time (t_s) under the gravity coefficient of 1000. It is worth noting that the holding time was the sum of the holding time in normal gravity plus the separation time in the supergravity field.

3.1.1. Effect of Separation Temperature

The alloy can be maintained in a solid/liquid coexistence state through semi-solid isothermal treatment during the melting of Al samples [25,26]. In this study, separation temperatures of 648 °C, 653 °C, and 658 °C were applied under the gravity coefficient G = 1000. This process allows for the preservation of the Fe-rich phase in the liquid phase while keeping the Al matrix predominantly in the solid phase. The macroscopic images of the samples obtained from these experiments are presented in Figure 4. Table 3 lists their corresponding experimental parameters, the chemical compositions of the filtered Fe contents, and the separation efficiencies. It is worth noting that even with the addition of the supergravity field, the Fe-rich impurities could not be filtered to the lower part of the crucible because the liquid fraction was too small, and the flow was significantly restricted through the mushy zone (boundary layer + Liquid phase) at T = 648 °C [16]. Therefore, no experimental liquid fraction could be separated (F_L = 0%) at this temperature [27]. As the separation temperature increased, the sample that was filtered to the lower part of the crucible increased significantly due to the elevated liquid fraction and flowability of the samples as shown in Figure 4b,c. At T = 653 °C, the F_L increased to 4.3%. However, when the separation temperature was increased to 658 °C, the Al phase began to melt, and the surface tension and the filtration resistance of the sample decreased, resulting in the mass of the Al liquid flowing into the lower part of the crucible with F_L = 50.2%. Furthermore, a cross-sectional comparison of the macroscopic morphology of the samples obtained from the lower crucible at different separation temperatures reveals interesting insights. At lower temperatures, the sample exhibits higher viscosity, retaining the characteristic trajectory of liquid phase filtration to the lower crucible. Conversely, at higher temperatures, the sample's viscosity decreases, resulting in a smoother disc-shaped appearance.

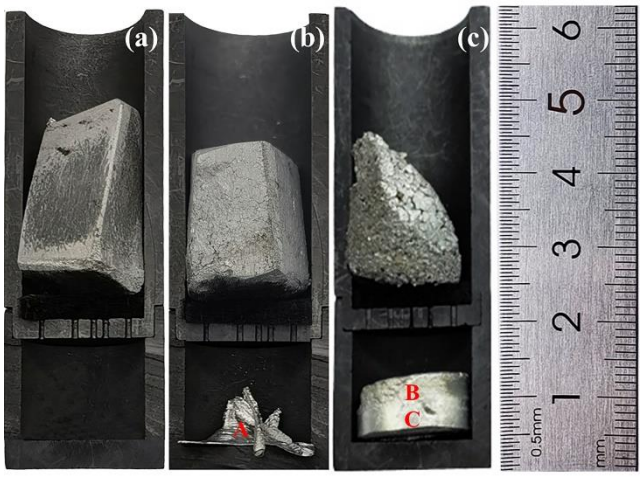


Figure 4. Macro diagram of the sample at t_h = 40 min, t_s = 3 min for different experimental temperatures: (**a**) 648 °C, (**b**) 653 °C, and (**c**) 658 °C.

Table 3. Experimental parameters and the corresponding chemical compositions of the filtered Fe contents and separation results at different temperatures.

Experimental Parameters			Separation Results			
T/°C	t_h/min	t_s/min	ω_{Fe_r}/wt.%	F_L/wt.%	R_{Al}/%	η_{Fe}/%
648	40	3	0.32	0	0	0
653	40	3	0.06	4.3	4.1	81.9
658	40	3	0.05	50.2	49.9	92.0

Figure 5 shows a line chart of the separation results at different experimental temperatures. It can be observed that as the temperature increased, the Fe content (ω_{Fe_f}) in the remaining Al decreased significantly, while the Fe removal rate (η_{Fe}) and the loss rate of the purified Al (R_{Al}) increased significantly. At T = 653 °C, the ω_{Fe_r}, η_{Fe} and R_{Al} achieved 0.06 wt.%, 81.9%, and 4.1%, respectively. Although the ω_{Fe_f} and η_{Fe} reached 0.05 wt.% and 92.0% at 658 °C, the R_{Al} reached 49.9%.

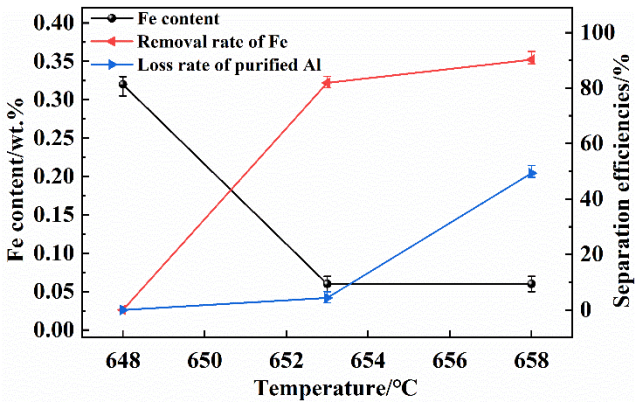


Figure 5. Line chart of the separation results at t_h = 40 min, t_s = 3 min for different experimental temperatures.

In order to observe the distribution of the composition in the filtered sample, the microstructure of the sample was studied under different separation temperatures, as shown in Figure 6. Figure 7a illustrates the microstructure of the sample filtered to the lower crucible at 653 °C. Figure 7b,c correspond to the microstructures of the upper and lower positions of the sample filtered to the lower crucible at 658 °C. It can be seen that

the sample was collected in the lower crucible, which mainly consisted of the Fe-rich phase [14]. As the separation temperature was increased, the amount of liquid phase in the treated sample increased, and the liquid of the Fe-rich phase carrying more and more Al matrix was filtered down into the lower part of the crucible, resulting in a decrease in the mass fraction of the Fe phase. Meanwhile, the Fe-rich phase was enriched along the direction of supergravity, forming a continuous network structure at the bottom, as shown in Figure 6b,c. This was because the density of the Fe-rich phase was greater than that of the Al melt. Thus, the separation temperature of 653 °C was chosen as the optimum temperature.

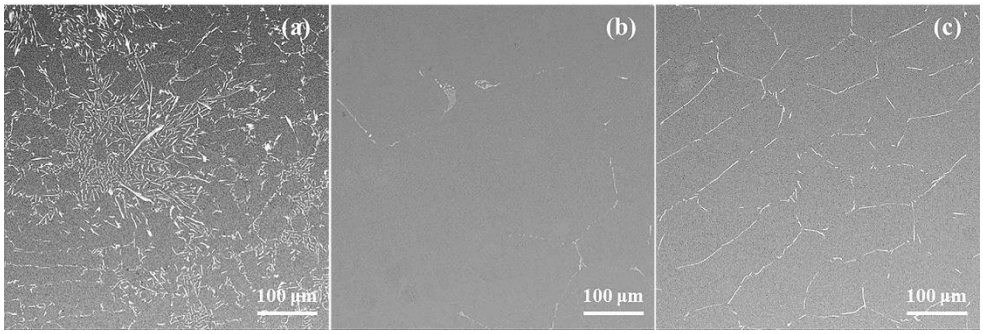


Figure 6. Microstructure of sample at t_h = 40 min, t_s = 3 min for different separation temperatures (corresponding to Figure 4 marked as "A–C"): (**a**) the sample filtered to the lower crucible at 653 °C, and the upper (**b**) and lower (**c**) positions of the sample filtered to the lower crucible at 658 °C.

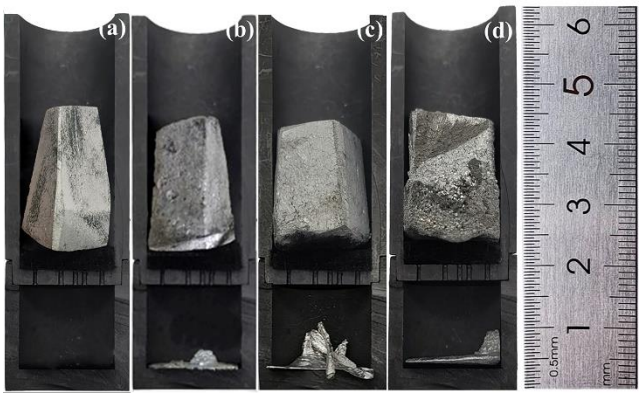


Figure 7. Macro diagram of the sample at T= 653 °C, t_s = 3 min for different holding times: (**a**) 20 min, (**b**) 30 min, (**c**) 40 min, and (**d**) 60 min.

3.1.2. Effect of Holding Time

Due to the high purity of metallic Al, a substantial number of impurities (Fe-rich phase) are present in the Al matrix. However, the diffusion rate of Fe in solid Al is relatively slow. To facilitate the movement of Fe-rich impurities from the matrix to the grain boundary and their separation out of the sample, the holding time is particularly crucial [28]. Figure 7 illustrates a macro diagram of the samples obtained with different holding times at T = 653 °C, t_s =3 min. Table 4 lists the corresponding experimental parameters, chemical compositions of the filtered Fe contents, and the separation efficiencies. Notably, the results of the experiment at the holding time of 20 min were similar to those in Figure 4a, where the Fe-rich phase could not be filtered to the lower part of the crucible, as increasing the holding time from 30 min to 60 min resulted in more and more samples being filtered into the lower part of the crucible. The F_L increased from 3.4% to 4.5%. The results indicate that irrespective of the holding time, the morphology of the sample in the upper crucible remains unchanged, displaying no noticeable collapse. Additionally, upon comparing the morphology of the samples obtained in the lower crucible, it is evident that with a

prolonged holding time, there is a substantial increase in the quantity of samples collected in the lower crucible. Furthermore, these samples gradually transition from an irregularly stacked configuration to a disc-shaped form. This transformation suggests that as the liquid phase content increases in the lower crucible samples over time, their viscosity decreases, and their fluidity is enhanced.

Table 4. Experimental parameters and the corresponding chemical compositions of the filtered Fe contents and separation efficiencies at different holding times.

Experimental Parameters			Separation Results			
t_h/min	t_s/min	T/°C	ω_{Fe_r}/wt.%	F_L/wt.%	R_{Al}/%	η_{Fe}/%
20	3	653	0.32	0	0	0
30	3	653	0.15	3.4	3.2	55.4
40	3	653	0.06	4.3	4.1	81.9
60	3	653	0.06	4.5	4.2	81.6

Figure 8 shows a line chart of the separation results at T = 653 °C, t_s = 3 min for different holding times. It can be seen that as the holding time was increased, the ω_{Fe_f} decreased significantly. The η_{Fe} increased significantly. However, when the holding time was greater than 30 min, the ω_{Fe_f} and η_{Fe} of the sample basically remained unchanged.

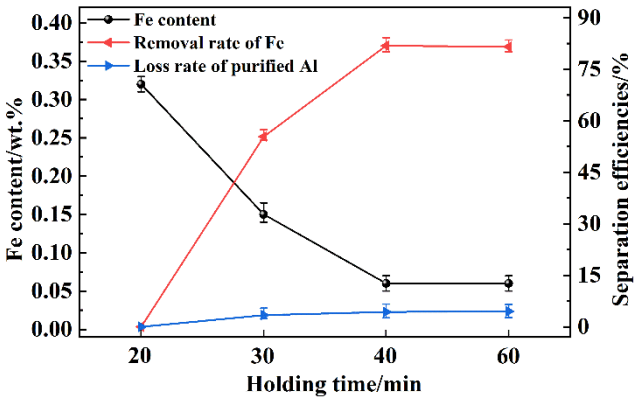


Figure 8. Line chart of the separation results at T = 653 °C, t_s = 3 min for different holding times.

The high-purity Al collected in the upper part from the different holding times was subjected to electron microscopic analysis at typical locations, as shown in Figure 9. At t_h = 20 min (Figure 9a), the results showed that during the sample melting process, the Fe-rich phase was essentially present as spherical eutectic particles in the sample compared to the raw material (Figure 2). This indicates that during the sample melting process, the Fe-rich phase dissolved, was broken, and spheroidized into small droplets before solidifying into the Al matrix at T = 653 °C. However, the Fe-rich phase could not be removed. When the holding time was increased, the amount of liquid phase in the grain boundaries increased and filtered to the lower part of the crucible, forming holes, as shown in Figure 9b–d. Meanwhile, it can be seen that the Fe-rich phase distributed in the Al matrix decreased, indicating that the Fe-rich phase in the Al matrix migrated to the grain boundary. At t_h = 40 min and 60 min (Figure 9c,d), only a very small amount of residual Fe-rich phase was distributed in the Al matrix, and almost all of the spheroidized Fe-rich phase in the Al matrix had migrated to the grain boundary. This is because the equilibrium distribution coefficient (k_0) value of Fe impurities is 0.03, which is defined as the ratio of impurity concentration in the solid (C_S) to that in the liquid (C_L). This means that the solubility of the Fe-rich phase in the solid phase is much smaller than that in the liquid phase [29,30]. It has been shown that Fe impurity elements at the solidification interface of the Al melt can be continuously moved to the liquid. Furthermore, the greater the

difference in the k_0 value of the impurity from 1, the more significant the purification effect. Here, the k_0 value of Fe impurities is much smaller than 1. Thus, the Fe-rich impurities in the Al matrix continuously migrate towards the liquid phase near the grain boundaries [29,31]. Ultimately, there is almost no presence of Fe-rich impurities in the Al matrix at t_h = 40 min and 60 min. Considering the separation efficiency and energy consumption comprehensively, t_h = 40 min was selected as the optimal holding time.

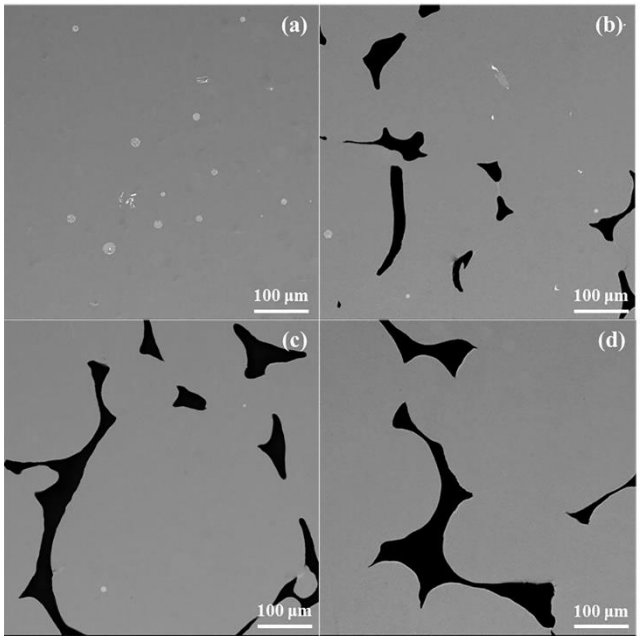


Figure 9. Microstructure of sample at T = 653 °C, t_s=3 min for different holding times: (**a**) 20 min, (**b**) 30 min, (**c**) 40 min, and (**d**) 60 min.

3.1.3. Effect of Separation Time

Figure 10 shows a macro diagram of the samples obtained at T = 653 °C and t_h = 40 min for different separation times. Table 5 lists the corresponding experimental parameters and the corresponding chemical compositions of the filtered Fe contents and separation efficiencies. When the separation time increased, more and more samples were filtered to the lower part of the crucible because the convection in the melt was enhanced, and the heat exchange was sufficient under the supergravity field, accelerating the filtering of the Fe-rich phase. The F_L was 3.9%, 4.3%, and 8.4% for separation times of 1 min, 3 min, and 5 min, respectively. Similarly, upon comparing the morphologies of the purified aluminum samples obtained in the upper crucible at different separation times, it is observed that with an increase in the separation time, a partial collapse occurs in the bottom part of the upper sample. Upon contrasting the morphology of the samples in the lower crucible, it is evident that with prolonged supergravity action, the filtered liquid, initially in a drip-like stacked configuration, gradually undergoes compression under supergravity, transforming into a disc-shaped structure. This indicates that prolonged exposure to supergravity can result in the overcoming of intermolecular forces, leading to the formation of strong convection and the attainment of a relatively dense solidified structure.

Figure 11 shows a line chart of the separation results at T = 653 °C and t_h = 40 min for different separation times. It can be observed that as the separation time increased from 1 min to 5 min, the ω_{Fe_f} decreased from 0.15 wt.% to 0.06 wt.%. Additionally, the values of η_{Fe} and R_{Al} increased from 55.0% to 83% and from 3.7% to 8.1%, respectively.

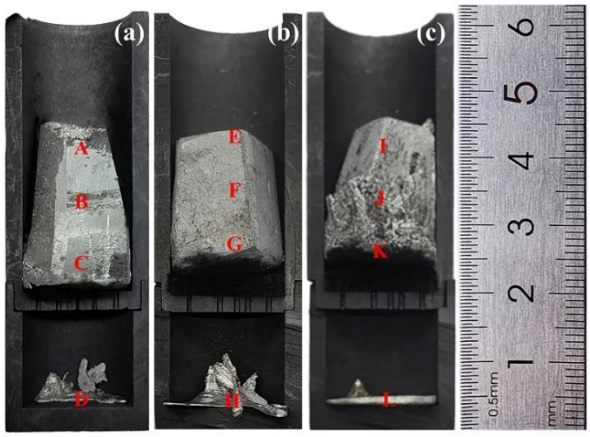


Figure 10. Macro diagram of the sample at T = 653 °C, t_h = 40 min for different separation times: (**a**) 1 min, (**b**) 3 min, and (**c**) 5 min.

Table 5. Experimental parameters and the corresponding chemical compositions of the filtered Fe contents and separation efficiencies at different separation times.

Experimental Parameters			Separation Results			
t_s/min	t_h/min	T/°C	ω_{Fe_r}/wt.%	F_L/wt.%	R_{Al}/%	η_{Fe}/%
1	40	653	0.15	3.9	3.7	55.0
3	40	653	0.06	4.3	4.1	81.9
5	40	653	0.06	8.4	8.1	83.0

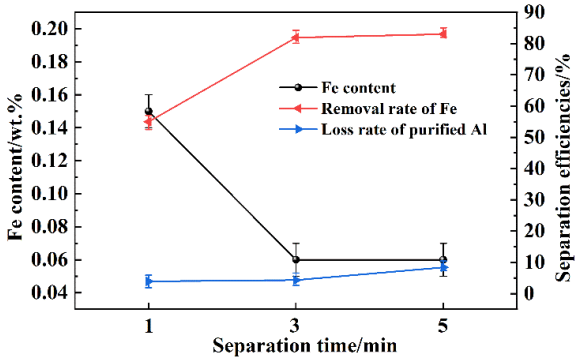


Figure 11. Line chart of the separation results at T = 653 °C, t_h = 40 min for different separation times.

Figure 12 illustrates the microstructure of the sample at T = 653 °C and t_h = 40 min under different separation times, where (a–l) correspond to Figure 10 at different positions marked "A–L" in red. After separation at T = 653 °C, t_h = 40 min for 1 min, along the supergravity direction, the grain boundary pores of the sample in the upper crucible initially increase and then decrease. This phenomenon can be attributed to the enrichment of the Fe-rich phase in the supergravity direction. Because the separation time was too short, the Fe-rich phase at the bottom did not have sufficient time to filter to the lower part of the crucible, resulting in smaller bottom pores. Moreover, a few residual spherical eutectic particles of the Fe-rich phase in the Al matrix can be observed. Upon increasing the separation time to 3 min, the grain boundary pores of the purified Al sample in the upper part of the crucible widened along the supergravity direction, as depicted in Figure 12e–g. This indicates that the separation time was appropriate for the Fe-rich phase along the grain boundary under these experimental conditions. The Fe-rich phase neither accumulates at the bottom of the Al sample (Figure 12c) nor results in excessively wide grain boundary pores due to excessive loss of the Al matrix (Figure 12i–k). Additionally, there was a noticeable decrease in the number of spherical eutectic particles in the Al matrix compared

to Figure 12a–c, demonstrating that increasing the separation time was beneficial for the immigration of the Fe-rich phase to the grain boundary from the Al matrix. Compared to Figure 12d,h,l, the concentration of the Fe-rich phase in the filtered sample initially increased and then decreased. This trend indicates that when the separation time exceeded 3 min, the proportion of the Al matrix in the sample filtered to the lower part of the crucible increased relative to that of the Fe-rich phase, resulting in an increase in the loss of Al, consistent with the results presented in Table 5. Thus, 3 min was chosen as the optimum separation time.

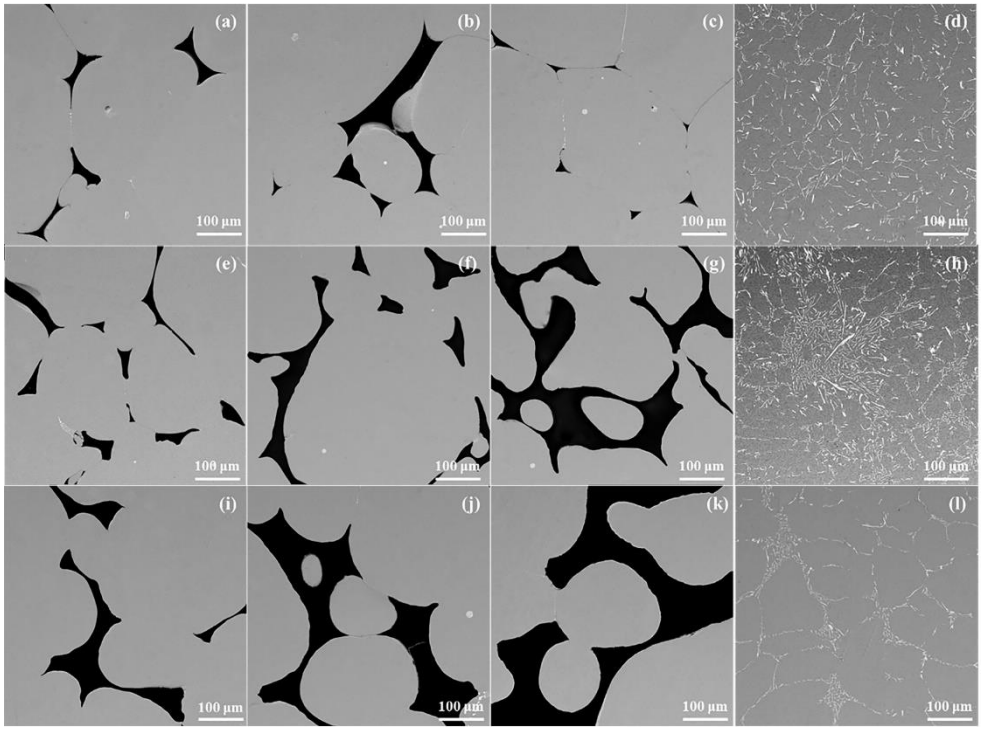


Figure 12. Microstructure of the sample at T = 653 °C, t_h = 40 min for different separation times (corresponding to Figure 10 marked as "A–L"): (**a**–**d**) 1 min, (**e**–**h**) 3 min, and (**i**–**l**) 5 min.

3.2. Removal Mechanism

According to the above experimental results, it can be seen that the method of purifying pure Al is similar to the mechanism of purification by unidirectional solidification/segregation, which is based on the fact that impurities have different solubility in the liquid or solid phases of metal [12,16]. The schematic diagram of the purification process using supergravity in the semi-solid state is shown in Figure 13. Impurity elements at the solidification interface of the melt can be continuously moved to the liquid or solid phase depending on their equilibrium distribution coefficient (k_0), that is, the greater the difference of the k_0 value of the impurity from 1, the more significant the purification effect. However, there is a variance between the k_0 and the actual distribution coefficient. Thus, the actual distribution coefficient is defined as the effective distribution coefficient (k_e). The melting–solidification equilibrium equation of the impurity elements in the purification process is as follows [13]:

$$k_e = \frac{k_0}{k_0 + (1 - k_0)e^{-\frac{R}{D}\delta}} \tag{5}$$

where D is the diffusion coefficient of the Fe, δ is the thickness of the boundary layer, and R is the speed of the crystal growth.

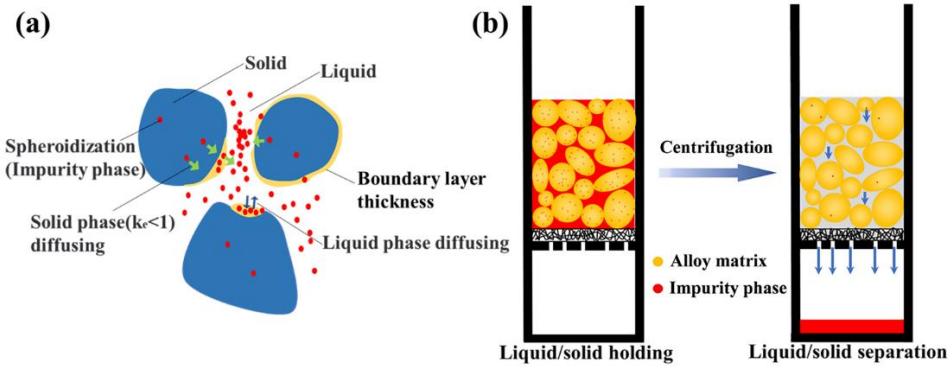


Figure 13. Schematic diagram of the purification process using supergravity in the semi-solid state: (**a**) sample melting process, (**b**) supergravity separation process.

The supergravity field can effectively increase the diffusion coefficient of the Fe (D) in the liquid phase, reduce the crystal growth rates (R), and decrease the boundary layer thickness (δ) [32]. By combining the above formulas, it can be observed that the effective distribution coefficient (k_e) is reduced, thereby improving the efficiency of Fe element migration from the solid phase to the liquid phase, as shown in Figure 13a. Additionally, the supergravity field increases the convection in the melt, facilitating the expulsion and transport of solutes and squeezing the liquid phase out of the Al matrix near the grain boundaries [22,23]. This reduces the Fe-rich phase in the liquid phase, ensuring a significant concentration difference between the solid and liquid phases. This, in turn, promotes the migration of the Fe-rich phase from the solid phase to the liquid phase near the grain boundaries, reducing the solute content (Fe-rich phase) in the solid phase. Therefore, this achieves the goal of purifying pure Al, as shown in Figure 13b. However, heightened metal purity corresponds to a more restricted semi-solid holding temperature interval, which means higher requirements for equipment temperature control.

4. Conclusions

This study investigated the impact of the separation temperature, holding time, and separation time on the loss rate of purified Al and the removal ratio of Fe elements. Simultaneously, the mechanism of supergravity in the semi-solid method of Al melt was discussed. The conclusions are summarized as follows.

1. The separation temperature significantly influences the loss rate of purified Al (R_{Al}), with a loss of only 4.1% at 653 °C and a substantial increase to 49.4% at 658 °C. The holding time has a notable impact on the removal rate of Fe (η_{Fe}) from the Al matrix. Specifically, at holding times of 20 min, 30 min, 40 min, and 60 min, the corresponding removal rates of Fe are 0%, 55.4%, 81.9%, and 81.6%, respectively. The separation time predominantly governs the removal rate of Fe (η_{Fe}) at the grain boundaries. At separation times of 1 min, 3 min, and 5 min, the corresponding removal rates of Fe are 55%, 81.9%, and 83%, respectively.

2. In the supergravity field, the Fe-rich phase at the grain boundary of the Al melt is preferentially filtered to the lower part of the crucible. At G=1000, T=653 °C, t_h=40 min, and t_s = 3 min, the loss rate of the purified Al reached 4.1%, and the Fe content was only 0.06 wt.% (the Fe content was 0.32 wt.% in the original material of pure Al). The removal rate of Fe was 81.9%.

3. The effective distribution coefficient (k_e) plays a crucial role in the purification of Al. Under the influence of the supergravity field, the value of k_e experiences reduction, thereby facilitating the migration of Fe impurities from the Al matrix to the grain boundary liquid phase. This process aids in the efficient separation of Fe impurities from the Al matrix under the supergravity field, consequently enhancing the overall purity of the final product.

Author Contributions: Methodology, L.W.; Software, L.W.; Validation, L.W., X.L., Z.W. and Z.G.; Formal analysis, L.W.; Investigation, Z.W.; Resources, Z.G.; Data curation, L.W., X.L. and Z.W.; Writing—original draft, L.W.; Writing—review & editing, X.L. and Z.G.; Visualization, L.W.; Supervision, X.L. and Z.G.; Project administration, Z.G.; Funding acquisition, Z.G. All authors have read and agreed to the published version of the manuscript.

Funding: This work was supported by the National Natural Science Foundation of China [grant number 52174275].

Data Availability Statement: The data presented in this study are available in article.

Conflicts of Interest: The authors declare that they have no conflicts of interest.

References

1. Matos, I.M.; Araújo, J.A.; Castro, F.C. Fretting fatigue performance and life prediction of 1120 aluminum alloy wires of overhead conductors. *Theor. Appl. Fract. Mech.* **2022**, *121*, 103521–103534. [CrossRef]
2. Rocha, P.H.C.; Langlois, S.; Lalonde, S.; Araújo, J.A.; Castro, F.C. Influence of 1350 and 6201 aluminum alloys on the fatigue life of overhead conductors-A finite element analysis. *Tribol. Int.* **2023**, *186*, 108661–108674. [CrossRef]
3. Li, Q.; Dai, T.; Gao, T.; Zhong, W.; Wen, B.; Li, T.; Zhou, Y. Aluminum material flow analysis for production, consumption, and trade in China from 2008 to 2017. *J. Clean. Prod.* **2021**, *296*, 126444. [CrossRef]
4. Czerwinski, F. Cerium in aluminum alloys. *J. Mater. Sci.* **2019**, *55*, 24–72. [CrossRef]
5. Tie, D.; Guan, R.; Wang, Z.; Fu, Y.; Zhang, J.; Chen, X.; Wang, Y.; Ling, C.; Cai, M. High electrical conductivity Al-Ag-Sc-Zr alloy with ultrafine grains processed by accumulative continuous extrusion. *Mater. Lett.* **2021**, *286*, 129227.1–129227.5. [CrossRef]
6. Wu, J.; Djavanroodi, F.; Gode, C.; Attarilar, S.; Ebrahimi, M. Melt refining and purification processes in Al alloys: A comprehensive study. *Mater. Res. Express.* **2022**, *9*, 032001–032018. [CrossRef]
7. Zhao, Q.; Qian, Z.; Cui, X.; Wu, Y.; Liu, X. Influences of Fe, Si and homogenization on electrical conductivity and mechanical properties of dilute Al–Mg–Si alloy. *J. Alloys Compd.* **2016**, *666*, 50–57. [CrossRef]
8. Kennedy, M.W.; Akhtar, S.; Bakken, J.A.; Aune, R.E. Electromagnetically Modified Filtration of Aluminum Melts-Part I: Electromagnetic Theory and 30 PPI Ceramic Foam Filter Experimental Results. *Metall. Mater. Trans. B* **2013**, *44*, 691–705. [CrossRef]
9. Wan, H.L.; Kong, L.X.; Yang, B.; Xu, B.Q.; Duan, M.P.; Dai, Y.N. Zone melting under vacuum purification method for high-purity aluminum. *J. Mater. Res. Technol.* **2022**, *17*, 802–808. [CrossRef]
10. Duan, M.; Zhao, J.; Xu, B.; Kong, L.; Yang, B.; Wan, H.; Fu, C. Study on the behavior of impurities in zone melting of aluminum. *J. Mater. Res. Technol.* **2022**, *21*, 3885–3895. [CrossRef]
11. Dewan, M.A.; Rhamdhani, M.A.; Mitchell, J.B.; Davidson, C.J.; Brooks, G.A.; Easton, M.; Grandfield, J.F. Control and Removal of Impurities from Al Melts: A Review. *Mater. Sci. Forum* **2011**, *693*, 149–160. [CrossRef]
12. Luo, Q.; Cong, M.; Li, H.; Zhu, L.; Chen, H.; Li, Q. Mechanism of Fe removal by Sn addition in Al-7Si-1Fe alloy. *J. Alloys Compd.* **2023**, *948*, 169724–169735. [CrossRef]
13. Wan, H.L.; Zhao, J.Y.; Yang, B.; Xu, B.Q.; Duan, M.P.; Kong, L.X.; Dai, Y.N. Study on the effective distribution coefficient of impurity separation in the preparation of high purity aluminum. *J. Mater. Res. Technol.* **2020**, *9*, 10366–10376. [CrossRef]
14. Wang, X.; Guan, R.G.; Misra, R.D.K.; Wang, Y.; Li, H.C.; Shang, Y.Q. The mechanistic contribution of nanosized Al_3Fe phase on the mechanical properties of Al-Fe alloy. *Mater. Sci. Eng. A* **2018**, *724*, 452–460. [CrossRef]
15. Mehrabian, R.; Geiger, D.R.; Flemings, M.C. Refining by Partial Solidification. *Metall. Trans.* **1973**, *5*, 785–786. [CrossRef]
16. Cho, T.T.; Sugiyama, S.; Yanagimoto, J. Effect of Process Parameters of Backward Extrusion by Servo Press on Purification of A7075 Alloy under the Semisolid Condition. *Mater. Trans.* **2016**, *57*, 1351–1356. [CrossRef]
17. de Moraes, H.L.; de Oliveira, J.R.; Espinosa, D.C.R.; Tenório, J.A.S. Removal of Iron from Molten Recycled Aluminum through Intermediate Phase Filtration. *Mater Trans* **2006**, *47*, 1731–1736. [CrossRef]
18. Ren, Y.; Chen, H.; Ma, W.; Lei, Y.; Zeng, Y. Purification of aluminium-silicon alloy by electromagnetic directional solidification: Degassing and grain refinement. *Sep. Purifi. Technol.* **2021**, *277*, 119459–119467. [CrossRef]
19. Choi, J.S.; La, M.; Kim, D.; Choe, K.-H.; Hyun, S.-K.; Kim, M.-J. Effect of electric current on the microstructural refinement of pure aluminum. *J. Mater. Res. Technol.* **2021**, *12*, 818–830. [CrossRef]
20. Lee, G.C.; Kim, M.G.; Park, J.P.; Kim, J.H.; Jung, J.H.; Baek, E.R. Iron Removal in Aluminum Melts Containing Scrap by Electromagnetic Stirring. *Int. Conf. Proc. Manu. Adv. Mater.* **2010**, *638–642*, 267–272. [CrossRef]
21. Liu, X.; Shuai, S.S.; Huang, C.L.; Wu, S.J.; Hu, T.; Chen, C.Y.; Wang, J.; Ren, Z.M. Microstructure and mechanical properties of directionally solidified Al-rich Ni_3Al-based alloy under static magnetic field. *J. Mater. Sci. Technol.* **2022**, *110*, 117–127. [CrossRef]
22. Sun, N.; Wang, Z.; Sun, B.; Li, Y.; Guo, Z. Purification of primary aluminum liquid through supergravity-induced filtration. *Chem. Eng. Technol.* **2022**, *182*, 109199–109212. [CrossRef]
23. Zhao, L.X.; Guo, Z.C.; Wang, Z.; Wang, M.Y. Removal of Low-Content Impurities from Al By Super-Gravity. *Metall. Mater. Trans. B* **2010**, *41*, 505–508. [CrossRef]
24. Seo, K.H.; Jeon, J.B.; Youn, J.W.; Kim, S.J.; Kim, K.Y. Recycling of Al-Si die casting scraps for solar Si feedstock. *J. Cryst. Growth* **2016**, *442*, 1–7. [CrossRef]

25. Wang, Y.F.; Zhao, S.D.; Zhao, X.Z.; Zhao, Y.Q. Effects of isothermal treatment parameters on the microstructure of semisolid alloys. *Mater. Sci. Technol.* **2018**, *34*, 104–110. [CrossRef]
26. Cho, T.T.; Meng, Y.; Sugiyama, S.; Yanagimoto, J. Separation technology of tramp elements in aluminium alloy scrap by semisolid processing. *Int. J. Precis. Eng. Manuf.* **2015**, *16*, 177–183. [CrossRef]
27. Bhagavath, S.; Cai, B.; Atwood, R.; Li, M.; Ghaffari, B.; Lee, P.D.; Karagadde, S. Combined Deformation and Solidification-Driven Porosity Formation in Aluminum Alloys. *Metall. Mater. Trans. A* **2019**, *50*, 4891–4899. [CrossRef]
28. Dám, K.; Vojtěch, D. Thermally stable Al-Fe-Mn-based alloy prepared by centrifugal spraying and hot die forging. *Mater. Sci. Eng. A* **2014**, *590*, 232–238. [CrossRef]
29. Avazkonandeh-Gharavol, M.H.; Haddad-Sabzevar, M.; Fredriksson, H. Effect of partition coefficient on microsegregation during solidification of aluminium alloys. *Int. J. Miner. Metall. Mater.* **2014**, *21*, 980–989. [CrossRef]
30. Pourgharibshahi, M.; Saghafian, H.; Divandari, M.; Timelli, G. Controlled Diffusion Solidification Pathway of an AA 7xxx Series Aluminum Alloy. *Metall. Mater. Trans. A* **2018**, *50*, 326–335. [CrossRef]
31. Cheung, N.; Bertazzoli, R.; Garcia, A. Experimental impurity segregation and numerical analysis based on variable solute distribution coefficients during multi-pass zone refining of aluminum. *J. Cryst. Growth* **2008**, *310*, 1274–1280. [CrossRef]
32. Li, R.X.; Wang, Z.; Guo, Z.C.; Liaw, P.K.; Zhang, T.; Li, L.; Zhang, Y. Graded microstructures of Al-Li-Mg-Zn-Cu entropic alloys under supergravity. *Sci. China Mater.* **2018**, *62*, 736–744. [CrossRef]

Disclaimer/Publisher's Note: The statements, opinions and data contained in all publications are solely those of the individual author(s) and contributor(s) and not of MDPI and/or the editor(s). MDPI and/or the editor(s) disclaim responsibility for any injury to people or property resulting from any ideas, methods, instructions or products referred to in the content.